

# A combined timing/spectral study of IRAS 13224-3809 using *XMM-Newton* data

M. D. Caballero-García<sup>1\*</sup>, I. E. Papadakis<sup>2,3</sup>, M. Dovčiak<sup>1</sup>, M. Bursa<sup>1</sup>,  
J. Svoboda<sup>1</sup>, V. Karas<sup>1</sup>

<sup>1</sup> *Astronomical Institute of the Czech Academy of Sciences, Boční II 1401, CZ-14100 Prague, Czech Republic*

<sup>2</sup> *Department of Physics and Institute of Theoretical and Computational Physics, University of Crete, 71003 Heraklion, Greece*

<sup>3</sup> *IA, FORTH, Voutes, GR-7110 Heraklion, Greece*

Accepted. Received; in original form

## ABSTRACT

We present the results from an X-ray variability study of IRAS 13224-3809. This is probably the best source for X-ray reverberation studies since it is X-ray bright, extremely variable, and it has been extensively observed with *XMM-Newton*. We used all the archival *XMM-Newton* data from the three EPIC cameras (to increase the signal-to-noise) and, given the many observations of the source, we were able to compute the time-lags spectra in three different flux levels/periods. We fitted the time-lags and energy spectra, simultaneously, using a new X-ray reverberation code which computes the time dependent reflection spectra of the disc as a response to an X-ray flash from a point source located on the axis of the black-hole (BH) accretion disc (lamp-post geometry). To the best of our knowledge, this is the first time for an AGN that both time-lags and energy spectra are fitted by a model simultaneously in different flux periods. The model fits in the case when the BH is rapidly rotating are significantly better than the model fits in the case of a Schwarzschild BH. This result strongly favours the hypothesis of a rotating central BH in this source. We also detect significant variations in the height of the X-ray corona. The X-ray height appears to increase from  $\sim 3 - 5$  gravitational radii when the X-ray luminosity is of the order of  $\sim 1.5 - 3$  percent of the Eddington limit, up to  $\sim 10$  gravitational radii, when the luminosity doubles.

**Key words:** black hole physics – galaxies: active – X-rays: galaxies.

## 1 INTRODUCTION

The most commonly accepted scenario for Active Galactic Nuclei (AGN) postulates that they are powered by accretion of matter onto a central super massive black hole (BH). AGN are strong X-ray emitters, probably via inverse Compton scattering of the optical/UV photons which are emitted from the accretion disc by hot electrons. The resulting X-ray energy spectrum has a power-law shape up to an energy characteristic of the electron temperature.

The X-ray source is believed to be located in the innermost part of the accretion disc since the X-ray luminosity is a sizeable fraction of the bolometric luminosity. It is also small in size, with radii not much larger than a few gravitational radii ( $r_g = GM_{\text{BH}}/c^2$ ;  $M_{\text{BH}}$  is the mass of the central BH). This is based on the high amplitude, fast variations that are observed in the X-ray emission from these objects. This is also supported by recent monitoring observa-

tions of several lensed quasars performed in the optical, UV, and X-ray bands (e.g. Chartas et al. 2016).

In bright AGN, with strong “big blue bump”, the disc probably extends down to the inner stable circular orbit, which implies that the X-ray source will be located at some height on top of it. If the X-ray emission is isotropic then it is unavoidable that the X-rays will illuminate the accretion disc. Part of the X-rays will be absorbed and will increase the temperature of the disc, and part of them will be “reflected”, giving rise to the so called X-ray reflection spectrum. The main features of this spectrum are: an excess of emission at energies below  $\sim 1 - 1.5$  keV (i.e. in the “soft” energy band), the presence of an iron line at  $\sim 6.4 - 7$  keV, and the broad “Compton hump” at energies  $\sim 20 - 50$  keV. Depending on the height of the X-ray source, the inner disc radius and its ionisation, these features will be affected by relativistic effects (e.g. the iron line will be broadened and the soft band emission will appear as a broad, featureless emission component). These features have been observed in the X-ray spectra of many AGN, although they may be explained in more than one way.

If X-ray irradiation of the inner disc takes place in AGN, we

\* E-mail: garcia@asu.cas.cz

expect to observe correlated variations in the X-ray continuum and the reflection components. The latter will be delayed, depending on the distance between the X-ray source and the accretion disc. Time delays between the soft band and the X-ray continuum variations were first reported in Ark 564 (McHardy et al. 2007), and were conclusively detected in 1H 0707-495 (Fabian et al. 2009). Since then, such delays have been detected in many more objects (Emmanoulopoulos et al. 2011; De Marco et al. 2013; Kara et al. 2016).

Theoretical modelling of the observed time-lags vs. frequency (i.e. the “time-lags spectra”) and of the time-lags, at a fixed frequency, as a function of energy have been performed a few times in the past (Cackett et al. 2014; Emmanoulopoulos et al. 2014; Epitropakis et al. 2016; Chainakun & Young 2015; Chainakun et al. 2016; Chainakun & Young 2017). Recently Caballero-García et al. (2018; G18 hereafter) studied the time-lags spectra of three AGN. They used a model which assumes a point-like X-ray source located at a height  $h$  above the BH (i.e. the so call “lamp-post” geometry; Matt et al. 1991) to fit the observed time-lags between the 0.3-1 and 1-10 keV bands. The model fitted the data well, and the best-fit height was  $\approx 4 r_g$ , on average, irrespective of the BH spin considered and the disc ionization. They also detected wavy-like residuals in the time-lags spectra at high frequencies, which suggest that the lamp-post model, in its simplest version, should be modified. Either the X-ray source is extended, or the height of the source varies with time.

IRAS 13224-3809 is a radio-quiet, X-ray bright, Narrow Line Seyfert 1 (NLSy1) galaxy, located at a luminosity distance of 310 Mpc (NED<sup>1</sup> database). It has been extensively studied in X-rays as it is one of the most variable Seyfert galaxies in this band, both in flux and spectral shape (i.e. Boller et al. 1997, 2003; Dewangan et al. 2002; Gallo et al. 2004; Ponti et al. 2010; Fabian et al. 2013; Chiang et al. 2015; Parker et al. 2018; Pinto et al. 2018; Jiang et al. 2018). *XMM-Newton* observed IRAS 13224-3809 in 2002, 2011 and 2016 for  $\sim 1$  day, 500 ks and 1.5 Ms, respectively. When combined together, these are among the longest *XMM-Newton* observations of a single AGN. Given the continuous, fast and large-amplitude variability of the source, they constitute a valuable data set to study the variability properties of the source in detail.

Kara et al. (2013), Emmanoulopoulos et al. (2014) and Chainakun et al. (2016) used the 2011 observation to study the time-lags spectrum versus frequency and energy of the source. Kara et al. (2013) studied the time-lags versus frequency spectra and found frequency and absolute amplitude variations between flaring and quiescent periods. They suggested that the X-ray source may be located closer to the accretion disc in the lower-flux than during the high flux period. Emmanoulopoulos et al. (2014) fitted the time-average time-lags versus frequency spectrum in the lamp-post geometry, and found that the X-ray source is located at  $\sim 3 r_g$  above the central BH. Chainakun et al. (2016) fitted both the time average time-lags versus energy and the energy spectrum with a similar model. They also found a small X-ray source height (of the order of  $2.0 r_g$ ).

Recently, Alston et al. (2019) used the full data set to study the variability properties of the source. They found strong evidence for non-stationarity. They showed that the rms-flux relation is not lin-

ear, and the power-spectrum density (PSD) normalisation increases with decreasing source flux, while the low-frequency peak moves to higher frequencies. Alston et al. (2020) used (almost) the same data to fit the time-lags spectra in time scales of the order of a day. They used the same model that G18 used, and found variations that could be explained if the height of the X-ray corona increases with increasing luminosity.

We present the results from a simultaneous spectral/timing study of IRAS 13224-3809. Like Alston et al. (2020) we use the full *XMM-Newton* data set but we consider both EPIC-pn and MOS data to reach the maximum possible signal-to-noise (S/N) ratio for the timing analysis. We also use an improved version of the model that G18 and Alston et al. (2020) used and we fit, simultaneously, both the time-lags versus frequency spectra and the energy spectrum. Our approach is similar to Chainakun & Young (2015, 2017) employed for another AGNs. Compared to the later authors, we use a longer data set, and we investigate the spectral/timing properties of the source in different flux levels (hereafter referred to as “periods” of time of IRAS 13224-3809 with similar fluxes). To the best of our knowledge, this is the first time that both the X-ray time-lags and energy spectrum of an AGN, in different flux periods, are fitted with a model that takes into account all the relativistic effects and the ionization radial profile of the disc.

## 2 DATA REDUCTION

We considered the three long *XMM-Newton* observations of IRAS 13224-3809 in 2002, 2011 and 2016 (Tab. 1 lists the observations log). The EPIC pn and MOS cameras were operating in the *Full Frame* and the *Large Window* imaging modes, respectively, during the 2002 and 2011 observations. They both operated in the *Large Window* mode during the 2016 observation. The *Thin* filter was used in the 2011 and 2016 observations, and the *Medium* filter in the 2002 observation. We processed the data from the EPIC-pn (Strüder et al. 2001) and the two MOS (Turner et al. 2001) cameras using the Scientific Analysis System (SAS) v. 16.1.0 (Gabriel et al. 2004).

EPIC-pn and MOS1, MOS2 source data were extracted using circular regions with a radius of 800 pixels ( $40''$ ) centred on the source coordinates as listed on the NASA/IPAC Extragalactic Database (RA =  $13^h 25^m 19.4^s$ , Dec =  $-38^d 24^m 52.6^s$ ) which were the same for the timing and the spectral analysis for each observation. We kept only events with PATTERN  $\leq 4$  and FLAG = 0 for the EPIC-pn data, and PATTERN  $\leq 12$  and FLAG = 0 for the MOS data. We assessed whether the observations are affected by pile-up using the SAS task *epatplot*, and we did not detect significant pile-up effects in any of them. Background data were extracted from large rectangular boxes far enough from the location of the source, but remaining within the boundaries of the same CCD chip (they were also the same for each observation for the timing and the spectral analysis, respectively).

We used the *Science Analysis System* (SAS) tool *evselect* to produce the source and background light curves in the 0.3-1 keV and 1-4 keV energy bands (the “soft” and “continuum” bands, respectively), using a time bin size of 100 s for all three cameras. Background subtracted light curves were produced using the SAS tool *epiclccorr*. We checked for background flaring events, and we removed data points where the background count rate was half or higher than the source rate, in both energy bands.

We summed the MOS1+MOS2 light curves (hereafter referred to as the MOS light curves) using the *lcmath* in *FTOOL*.

<sup>1</sup> The NASA/IPAC Extragalactic Database (NED) is funded by the National Aeronautics and Space Administration and operated by the California Institute of Technology.

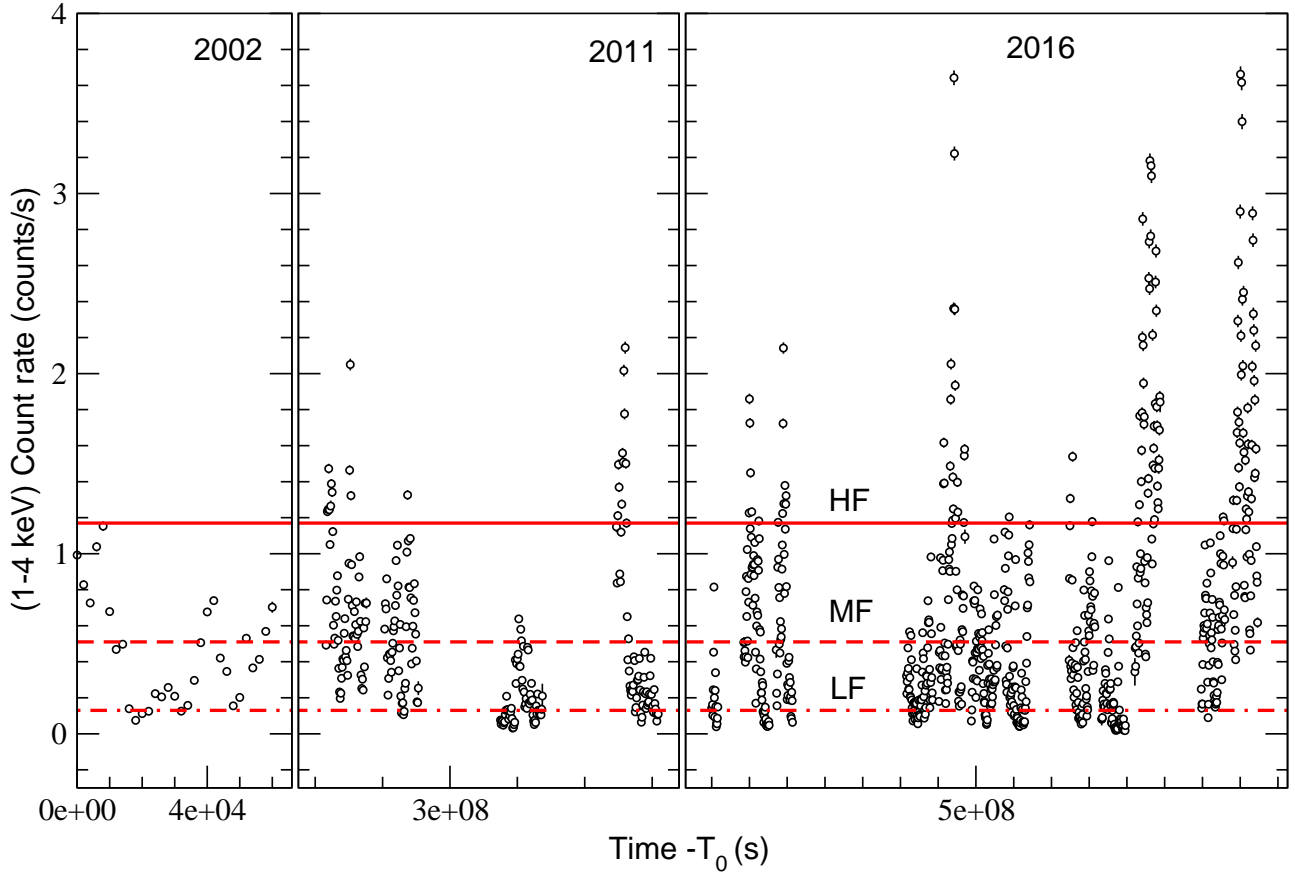


**Figure 1.** The EPIC pn+MOS, 1-4 keV band light curve, binned in 2 ks. Time is measured in seconds since the start of the 2002 observation. The solid, dashed and dot-dashed horizontal lines indicate the count rate limits of the “HF”, “MF” and “LF” periods (see text for details).

**Table 1.** *XMM-Newton* observations log.

Date Obs. (dd/mm/yyyy)	Obs. ID	Duration (s)
19/01/2002	0110890101	64019
19/07/2011	0673580101	133039
21/07/2011	0673580201	132443
25/07/2011	0673580301	129438
29/07/2011	0673580401	134736
08/07/2016	0780560101	141300
10/07/2016	0780561301	141000
12/07/2016	0780561401	138100
20/07/2016	0780561501	140800
22/07/2016	0780561601	140800
24/07/2016	0780561701	140800
26/07/2016	0792180101	141000
30/07/2016	0792180201	140500
01/08/2016	0792180301	140500
03/08/2016	0792180401	140800
07/08/2016	0792180501	138000
09/08/2016	0792180601	136000

Then we added the pn with the MOS light curve, producing the final light curves in the two energy bands. Before adding the light curves, we divided one over the other, to check whether their ratio was stable and consistent with a constant. This was the case almost

always (except for a few, short, light curve parts at the beginning and/or the end of each observation, which we ignored).

The final light curves cover periods when both instruments were operating. They contain a small number of missing points ( $\leq 5\%$  of the total number of points in each light curve). They are randomly distributed throughout the duration of an observation, or appear in groups of  $\leq 10$  points (maximum). We replaced the missing points by a linear interpolation, with the addition of the appropriate Poisson noise.

In Fig. 1 we show the final, pn+MOS, 1-4 keV light curve binned to 2 ks. In the following section we describe the way we estimated the time-lags in the three “flux periods”, namely the “High-flux (HF)”, the “Medium-flux (MF)”, and the “Low-flux (LF)” periods. The horizontal lines in Fig. 1 at  $0.13$ ,  $0.51$  and  $1.17 \text{ s}^{-1}$  indicate the count rate limits that we used to define these periods. We used the 1-4 keV band to define the flux periods, because this band should be more representative of the primary X-ray emission.

For the energy spectral analysis we used the EPIC-pn camera only, for simplicity and to avoid possible issues due to cross-calibration effects between the pn and MOS cameras. We chose the EPIC-pn camera because it has a larger effective area (i.e. double) than each one of the MOS cameras. We built response matrix functions with the SAS tasks `rmfgen` and `arfgen`. We used `evselect` to produce three EPIC-pn energy spectra for each observation identifier (OBSID), i.e. one for each LF, MF and HF periods, using the start and end time of all the light curve segments that we used to

construct the LF, MF and HF light curves. We combined the individual spectra using the `epicspeccombine` task, and we created the final LF, MF and HF, source and background spectra. The spectra were rebinned using the `grppha` task to have at least 200 counts for each background-subtracted spectral bin.

### 3 TIME-LAGS ESTIMATION

We used the method proposed by Epitropakis & Papadakis (2016, EP16 hereafter) to estimate the time-lags between the 0.3-1 keV and 1-4 keV light curves. A detailed description of the method is given in EP16. We summarise below the main points, for consistency and clarity.

First, we divided the light curves into segments of duration  $T = 10$  ksec. Each segment was placed into the HF, MF or LF periods, if its mean count rate in the 1-4 keV band was larger than 1.17, between 0.51-1.17 and between 0.13-0.51 counts/s, respectively (see Fig. 1). There are  $m = 80, 60$  and  $27$  segments in the LF, MF and HF periods, respectively. We calculated the cross-periodogram of all the HF, MF and LF segments at frequencies  $\nu_p = p/(N\Delta t)$  ( $p = 1, \dots, N/2, N = 100$ , and  $\Delta t = 100$  s, in our case). Our cross-spectrum and time-lag spectrum estimates are,

$$\hat{C}_{xy}(\nu_p) = \frac{1}{m} \sum_{k=1}^m I_{xy}^{(k)}(\nu_p), \quad (1)$$

and

$$\hat{\tau}_{xy}(\nu_p) \equiv \frac{1}{2\pi\nu_p} \arg[\hat{C}_{xy}(\nu_p)], \quad (2)$$

respectively ( $I_{xy}^{(k)}(\nu_p)$  is the cross-periodogram of the  $k$ -th segment at frequency  $\nu_p$ ). The error of  $\hat{\tau}_{xy}(\nu_p)$  is given by:

$$\sigma_{\hat{\tau}}(\nu_p) \equiv \frac{1}{2\pi\nu_p} \frac{1}{\sqrt{2m}} \sqrt{\frac{1 - \hat{\gamma}_{xy}^2(\nu_p)}{\hat{\gamma}_{xy}^2(\nu_p)}}, \quad (3)$$

where,

$$\hat{\gamma}_{xy}^2(\nu_p) \equiv \frac{|\hat{C}_{xy}(\nu_p)|^2}{\hat{P}_x(\nu_p)\hat{P}_y(\nu_p)}. \quad (4)$$

$\hat{P}_x(\nu_p)$  and  $\hat{P}_y(\nu_p)$  are the traditional periodograms of the two light curves, which are also calculated by binning over  $m$  segments, and  $\hat{\gamma}_{xy}^2(\nu_p)$  is the sample coherence function (defined on the interval  $[0, 1]$ ).

Fig. 2 shows the HF, MF and LF time-lags spectra (top panel) and the respective coherence functions (bottom panel). The time-lags in the three flux periods appear rather similar. They become negative at around  $\sim 3 \times 10^{-4}$  Hz and then broadly approach and cross zero at frequencies higher than 0.002 Hz. The coherence decreases to zero at high frequencies due to the Poisson noise effects (but also due to intrinsic reason; see EP17). The loss of coherence at high frequencies can be reasonably well approximated by an exponential function of the form (EP16),

$$\hat{\gamma}_{xy}^2(\nu) = \left(1 - \frac{1}{m}\right) \exp[-(\nu/\nu_0)^q] + \frac{1}{m}. \quad (5)$$

The solid, smooth black, blue and red curves in the bottom panel of Fig. 2 show the best-fit model lines to the HF, MF and LF coherence. The vertical lines in the same panel indicate the frequency at which the best-fit coherence functions are equal to  $1.2/(1 + 0.2m)$ . This is the maximum frequency,  $\nu_{\max}$ , at which

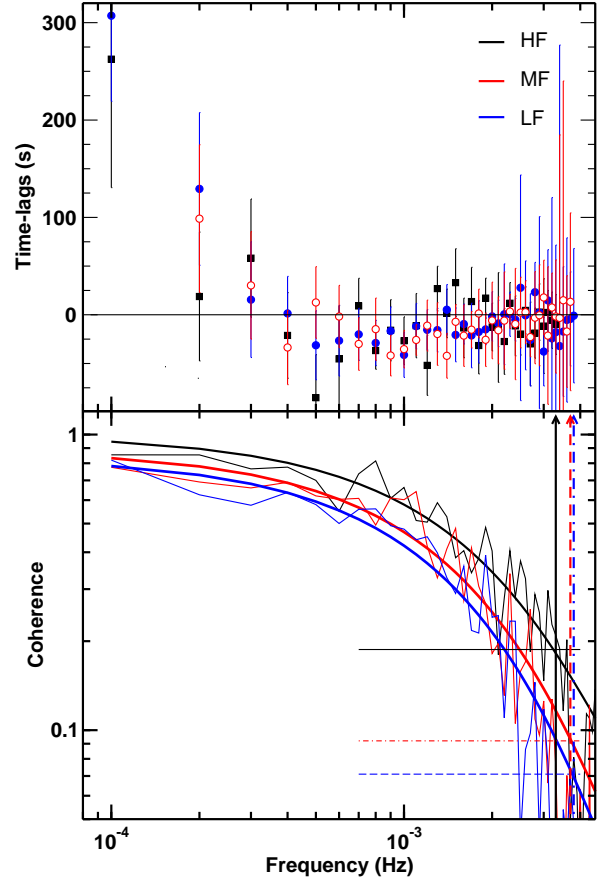


**Figure 2.** The HF, MF, and LF time-lags spectra (top panel; filled squares, open and filled circles, respectively) and the respective coherence functions (bottom panel; data are connected by black, red and blue solid lines, from the top to the bottom, respectively). The solid black, dashed red and dot-dashed blue vertical lines in the bottom panel indicate the highest frequency up to which we can estimate the HF, MF and LF time-lags, respectively (see text for details).

we can reliably estimate time-lags. Above  $\nu_{\max}$ , the time-lag estimates are biased (they converge to zero, irrespective of their true value) and eq. 3 underestimates their true error. In our case,  $\nu_{\max, \text{HF}} = 3.3 \times 10^{-3}$  Hz, and  $\nu_{\max, \text{MF, LF}} \sim 3.7 \times 10^{-3}$  Hz. So we decided to keep the time-lags spectra up to  $3.3 \times 10^{-3}$  Hz only, for all flux periods.

In order to increase the signal-to-noise ratio of the time-lags, we smoothed them by binning consecutive time-lag estimates. We did not bin the three lowest frequency points (to constrain the low frequency, positive, hard lags as much as possible) and we used bins of size 3 and 6 at higher frequencies. The resulting time-lags spectra appear in Fig. 3. Soft, negative time-lags are clearly observed for almost a decade in frequency (from  $\sim 3 \times 10^{-4}$  up to 0.002 Hz). We used the binned time-lags shown in this figure in the model fitting process we present below.

## 4 MODEL FITTING AND RESULTS

### 4.1 Initial considerations

Due to its long *XMM-Newton* observations, IRAS 13224-3809 is the only AGN that we can compute the time-lags at various flux

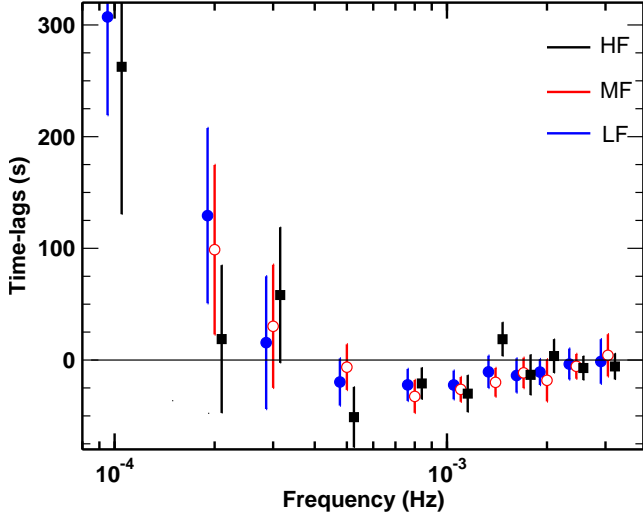


**Figure 3.** The binned HF, MF, and LF time-lags spectra (filled squares, open and filled circles, respectively). The HF and the LF time-lags are shifted in frequencies by a factor of 1.1 and 0.9, respectively, for clarity reasons.

periods, with a reasonable accuracy. This possibility offers us additional information that we can use to determine important physical parameters of the source, like the BH spin and the source height for example. However, even in this case, this is not an easy task. This is due to the fact that the observed time-lags depend on many parameters, like the BH mass, source height (and size, in practice), disc ionization, iron abundance and inclination of the disc, BH spin, etc. In principle, we could also estimate the 5-7 vs. 1-4 keV band time-lags (i. e. the time-lags between the iron-line and the continuum variations) and fit, simultaneously, both the soft and the iron line time-lags spectra, to determine the model parameters with higher accuracy. However, this cannot be done in IRAS 13224-3809. The source has a steep X-ray spectrum, and the count rate at energies above  $\geq 5$  keV is very low. As a result, it is not possible to compute the iron-line time-lags spectra with any reasonable accuracy, even if we consider the full data set (if we split the light curves in various flux periods).

There is a consensus in the scientific X-ray community that (whenever it is possible) it is important to study spectral and timing data together to consistently and accurately determine the physical parameters of the disc/corona geometry. We decided to follow this approach<sup>2</sup> and present it here. So we fit the time-lags versus frequency simultaneously with the energy spectrum of the source.

The full band X-ray spectrum of IRAS 13224-3809 is notoriously complicated (see e.g. Jiang et al. 2018 for an analysis of the X-ray spectrum in the full 0.3-10 keV *XMM-Newton* pass-band during the 2016 observation). In addition to the continuum and the X-ray reflection components, spectral features due to warm absorbing material as well as extra broad spectral components in the soft band can also be observed. In order to keep our modelling as less affected from these additional components as possible, we decided to fit the time-lags spectra plotted in Fig. 3 together with the HF, MF and LF energy spectra in the 3-10 keV band. According to Fig.

10 of Jiang et al. (2018), the main components in the energy spectrum of the source at energies 3 – 10 keV are the continuum and the reflection component(s) with the prominent iron line feature. So, the time-lags between the 0.3-1 vs. 1-4 keV band light curves hold information regarding the reverberating X-ray reflection spectrum in the soft band while the energy spectrum in the 3-10 keV band is representative of the reflection signal in the iron line band.

## 4.2 The model fitting process

We fitted both the time-lags and the energy spectra, simultaneously, in the three flux periods. We ignored the data in the energy range 7.5 – 8.3, 7.5 – 8.3 and 7.5 – 8.1 keV for the LF, MF and HF energy spectra, respectively, due to the absorption features that appear in these bands (e.g. Parker et al. 2017; Chartas & Canas 2018).

We used the KYNXILREV<sup>3</sup> model to fit the time-lags spectra. This is almost identical to the KYNREFREV model that we used in G18, with the exception that, in this version, re-processing of the ionised disc is computed using the XILLVER tables (García & Kallman 2010; García et al. 2013). As for fitting the energy spectra, we used the KYNXILLVER model, which is part of the KYN<sup>4</sup> set of models first presented in Dovčiak et al. (2004) and later in Dovčiak et al. (2014b). KYNXILREV can fit both time-lags and energy spectra. However, KYNXILLVER is much faster in fitting energy spectra, and since both models are identical (in the assumed geometry, relativistic and X-ray reflection modelling) we decided to use the later for fitting the energy spectra.

Both KYNXILREV and KYNXILLVER assume the so called lamp-post geometry. The X-ray source is assumed to be point-like, located on the axis of the black-hole accretion disc system, at a height  $h$  above the BH. The X-ray continuum spectrum is of the form:  $F(E) \propto E^{-\Gamma} e^{-E/E_c}$ , where  $E_c = 300$  keV. The X-ray source is assumed to emit isotropically, in its own frame, and the models take into account all the relativistic effects in the propagation of light from the primary source to the disc and to the observer, and from the disc to the observer. The models assume a thin, Keplerian disc, co-rotating with the BH. The inner disc edge is equal to the radius of the innermost stable circular orbit,  $r_{ISCO}$ , and the outer radius,  $r_{out}$ , is fixed at  $10^3 r_g$ . The inner disc radius is determined by the BH spin. The ionisation state of the disc changes with radius and depends on the illuminating pattern (of the continuum as it illuminates the disc) as well as on the density radial profile of the disc. In order to model the reflection spectrum we used the XILLVER tables (García et al. 2016) to be able to allow the disc density to be a variable parameter during the model fits. However, we assumed (for simplicity) a constant density radial profile.

One of the main physical parameters of both models is the BH mass,  $M_g$  (in units of  $10^8 M_\odot$ ). We kept it fixed to  $2 \times 10^6 M_\odot$  during the model fitting<sup>5</sup>. This was made in order to be able to determine the height of the X-ray source as accurately as possible. The X-ray source height and the BH mass affect the time-lags in a similar way. Therefore, if the BH mass in IRAS 13224-3809 is larger/smaller than the adopted BH mass then the source height (in

<sup>3</sup> <https://projects.asu.cas.cz/stronggravity/kynreverb>

<sup>4</sup> <https://projects.asu.cas.cz/stronggravity/kyn>

<sup>5</sup> This BH mass estimate is based on the results from the recent study of X-ray reverberation properties of IRAS 13224-3809 (Alston et al. 2020) and the results of the study of its PSD from Alston et al. (2019) using the relationship between PSD break timescale, black hole mass and luminosity from McHardy et al. (2006).

<sup>2</sup> This decision was made after performing timing and spectroscopy separately and confirming that the results are consistent with the ones presented in this paper.

gravitational radii) should be smaller/larger than our best-fit estimates, proportionally. However, the BH mass value cannot affect any relative changes between the best-fit  $h$  values in the three flux periods.

Another important physical parameter is the BH spin,  $a$ , which defines  $r_{\text{ISCO}}$ . When measured in geometrized units,  $a$  can attain any value between zero for a Schwarzschild BH (in which case  $r_{\text{ISCO}} = 6r_g$ ), and 1 in the case of a co-rotating disc around a rapidly spinning BH (in which case  $r_{\text{ISCO}} = 1r_g$ ). Although the light curves from IRAS 13224-3809 are very long, they are still not good enough to constrain the spin of the source with a high accuracy (even if we fit simultaneously time-lags and energy spectra). For that reason, following G18, we decided to fit the data in the two extreme cases of  $a = 0$  or  $a = 0.99$ . In this way, we wish to investigate whether the existing spectral/timing data can discriminate between a non-rotating and a rapidly rotating BH. We used a value for the inclination of the accretion disc of  $\theta_0 = 45^\circ$ , i.e. an intermediate value.

The KYNXILREV model includes a phenomenological, power-law-like prescription for the hard (i.e. positive) time-lags at low frequencies, of the form:

$$\tau(\nu) = A\nu^{-s}. \quad (6)$$

The power-law-like assumption of the low-frequency positive lags is a good description of the observed time-lags in various energy bands of many AGN (e.g. Epitropakis & Papadakis 2017).

During the fitting process we obtain the observed primary isotropic fluxes in the 2-10 keV energy range, in units of the Eddington luminosity ( $L_{\text{EDD}} = 2.5 \times 10^{44} \text{ erg s}^{-1}$  for the adopted BH mass shown in Tab. 2). Additionally, we fix the spectral normalization value to  $1.04 \times 10^{-5}$ . The latter is the normalization of the *kynxillver* model (defined as  $\text{norm} = 1/D^2$ , where  $D$  is the distance to the source in Mpc). This value was set according to the luminosity distance of the source, i.e. 310 Mpc.

We note that we also tested for the effects of possible absorption by an extended outflow (Pinto et al. 2018) to the validity of our fit results. If the absorption is by highly ionized material and it is uniform at energies above 3 keV, then it will mainly affect the estimation of the intrinsic X-ray luminosity. To verify this, we set the *kynxillver* normalization to be equal to  $5.2 \times 10^{-6}$ . This is half the value we mentioned in the previous paragraph, and it corresponds to the case when the observed flux is halved due to absorption. We fitted the data (time-lags and energy spectra), and the quality of the best-fit turned to be the same as before (i.e. the best-fit  $\chi^2$  values for the two spin parameters were almost identical to the values listed in Tab. 2). The best fit values were also very similar to the values listed in Tab. 2, except of  $L_{2-10}/L_{\text{Edd}}$ , which was doubled, and the disc density that was approximately 1.5 times larger.

The model parameters that we let free to vary during the model fits are the following: the iron abundance (with respect to the solar,  $Z/Z_\odot$ ), the disc density, the height of the X-ray source ( $h$ , in units of  $r_g$ ), the observed primary X-ray flux in the 2-10 keV band ( $L_{2-10}$ , in units of the Eddington luminosity,  $L_{\text{Edd}}$ ) and the spectral slope ( $\Gamma$ ). We also let the normalization and slope ( $A$  and  $s$ ) of the power-law model for the positive (continuum) time-lags to be free parameters during the model fits but we kept them to be the same in all flux periods. In any case, the fits do not improve if we let either the normalization  $A$  and/or the slope,  $s$ , to be different in each flux period.

**Table 2.** Best-fit parameters using the models *kynxillrev* and *kynxillver* when we fit the time-lags and the energy spectra, respectively. We used a rapidly and zero spin values (left and right column, respectively). Errors indicate the 68 % confidence intervals.

$a$	0.99	0.0
Parameters common to all three flux periods		
$Z/Z_\odot$	$4.9^{+3}_{-0.4}$	$4.3^{+0.8}_{-0.9}$
Density ( $10^{15} \text{ cm}^{-3}$ )	$2500^{+1800}_{-150}$	$2200^{+900}_{-800}$
$A(\text{sec})$	$(4.5 \pm 1.0) \times 10^{-5}$	$(4.9 \pm 1.0) \times 10^{-6}$
$s$	$1.7 \pm 0.3$ (t)	$1.9 \pm 0.4$ (t)
LF period		
$h$ ( $r_g$ )	$3.4^{+0.9}_{-0.7}$	$4.7^{+2.3}_{-2.5}$
$\Gamma$	$1.91^{+0.07}_{-0.06}$	$1.82^{+0.04}_{-0.06}$
$L_{2-10}/L_{\text{Edd}}$	$(1.44^{+0.06}_{-0.10}) \times 10^{-2}$	$(1.68 \pm 0.05) \times 10^{-2}$
MF period		
$h$ ( $r_g$ )	$5.4^{+1.7}_{-1.0}$	$8.4^{+3.9}_{-2.9}$
$\Gamma$	$2.38^{+0.04}_{-0.05}$	$2.32^{+0.02}_{-0.06}$
$L_{2-10}/L_{\text{Edd}}$	$(2.71^{+0.08}_{-0.05}) \times 10^{-2}$	$(2.92^{+0.04}_{-0.03}) \times 10^{-2}$
HF period		
$h$ ( $r_g$ )	$9.7^{+10}_{-0.8}$	$9.7^{+0.8}_{-0.8}$
$\Gamma$	$2.69^{+0.04}_{-0.12}$	$2.65^{+0.13}_{-0.05}$
$L_{2-10}/L_{\text{Edd}}$	$(5.45 \pm 0.15) \times 10^{-2}$	$(5.41^{+0.11}_{-0.21}) \times 10^{-2}$
$\chi^2/\nu$	1.13 (469/414)	1.18 (487/414)
p-value	0.032	$7.8e - 3$

### 4.3 The best-fit results

We fitted, simultaneously, both the time-lags and the energy spectra of the three flux periods twice: once assuming  $a = 0$  and the second time fixing the spin parameter to 0.99. The model fitting of the time-lags and the energy spectra was done in XSPEC 12.9.0 (Arnaud et al. 1996). The best fit results are reported in Tab. 2 (middle and right columns for the  $a = 0.99$  and  $a = 0$  model fits, respectively). The best fit models are shown in Fig. 4 (time-lags and energy spectra are plotted in the left and right panels, respectively). The cases of a Schwarzschild and a rapidly rotating BH are shown in the top and the bottom panels, respectively.

Both the  $a = 0$  and the  $a = 0.99$  best-fit probability values are rather low. The poor quality of the model fits is mainly due to the best-fit residuals that appear at energies below  $\sim 3.3$  keV in the LF energy spectra (possibly due to the presence of a blue-shifted, S XVI absorption line at these energies, e.g. Jiang et al. 2018). Indeed, if we neglect the points below 3.3 keV in the energy spectra the best-fit improves significantly, with  $\chi^2 = 430.8$  and 439.8 for 403 d.o.f. when  $a = 0.99$  and 0, respectively. We furthermore investigated if we can get a better fit by allowing the inclination to be a free parameter. The best fit inclination values are  $47.5^\circ \pm 1.8$  and  $42.0^{+2.5}_{-1.7}$  for the  $a = 0.99$  and 0 cases, respectively. These values are similar to the one we had originally assumed ( $45^\circ$ ). Since the fit does not improve significantly ( $\Delta\chi^2 \sim 2 - 3$  for 414 d.o.f.) and the new model parameter values are consistent (within the errors) with the previous ones, we decided to keep the original best-fit results.

Looking at the residuals of the best-fits to the time-lags (left column panels in Fig. 4), we can see that the  $a = 0$  model cannot fit the observed time-lags as good as the  $a = 0.99$  model. The best-fit



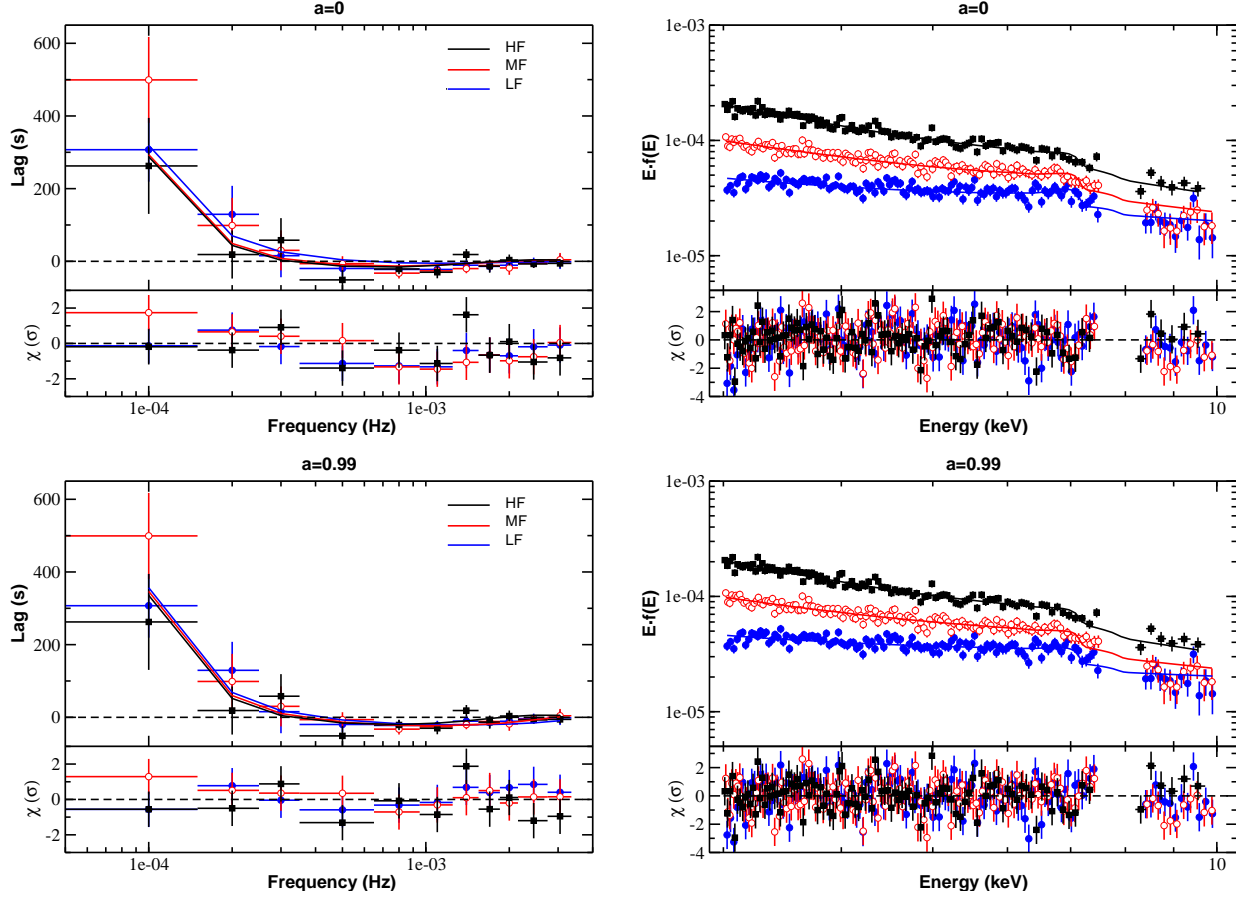


**Figure 4.** The (0.3-1 versus 1-4 keV) X-ray soft time-lag versus frequency (left) and (3-10 keV) energy spectra (right) fitted with the *kynxilrev* and *kynxillver* models, respectively, using the same values of the parameters obtained for spin zero (top) and rapidly spinning (bottom) from Tab. 2.

$a = 0$  model appears to be consistently overestimating the time-lags at frequencies higher than  $\sim 3 \times 10^{-4}$  Hz. As a result,  $\Delta\chi^2 = 10$  between the best-fit of the  $a = 0.99$  and the  $a = 0$  model to the time-lags only ( $\Delta\chi^2 = 18$  when we consider the energy spectra as well). It is difficult to quantify the improvement in the quality of the best-fit in the high-spin case, one reason being that the number of degrees of freedom (hereafter d.o.f.) is the same in both model fits. One way to do so is to compute the “ratio of likelihoods”, which is equal to  $e^{\Delta\chi^2/2}$  (Mushotzky 1982). In our case, this is identical to the “evidence ratio”, which is based on the Akaike (Akaike 1973) information criterion (see eq. 8 in Emmanoulopoulos et al. 2016). This ratio is a measure of the relative likelihood of one versus the other model, and is equal to  $\sim 150$  in our case ( $\sim 8100$  when we consider the energy spectra as well). This result does not mean that we can reject the hypothesis that the spin zero model is correct, but it does mean that the high spin model is much “more likely” (i.e. many hundreds to thousand times) to be the “real/correct” model. We therefore conclude that our results strongly support the hypothesis of a rapidly-rotating BH in IRAS 13224-3809.

The best-fit iron abundance and disc density values are consistent with the results from Jiang et al. (2018), who performed a detailed spectral analysis of the 2016 observations using a similar model to ours. The best-fit spectral slopes become steeper with increasing source flux, as commonly observed in AGN. Our results show that the height of the X-ray source in IRAS 13224-3809 is not constant. Instead, we find that the height should increase with

increasing flux. According to our best-fit results, the X-ray source height increases from  $\sim 4 r_g$  in the LF period to almost  $\sim 10 r_g$  in the HF period. This trend of higher height of the corona with increasing X-ray luminosity is in agreement with the recent results of Alston et al. (2020), to the time-lags only. The best-fit height values we find are systematically smaller than the best-fit results of Alston et al. (2020). This is due to the fact that we use a different reflection model, and our best-fit disc density is almost 3 order of magnitude larger than the disc density that Alston et al. (2020) assumed in their model fitting. As a result, for the same X-ray luminosity, the disc in our case will be less ionized, and the reflection fraction will be smaller (for a given height). Consequently, the best-fit height is lowered, to achieve a reflection fraction similar to the one for a less dense disc and an X-ray source at a larger distance from the disc.

## 5 DISCUSSION AND CONCLUSIONS

We present the results from a combined study of the X-ray time-lag and energy spectra of IRAS 13224-3809, which is one of the most variable and most observed NLSy1 AGN galaxies with *XMM-Newton*. For the timing analysis we used the data from EPIC-pn and the two MOS cameras on-board *XMM-Newton* to maximize the signal, whilst for the energy spectra we used the data from the EPIC-pn only. We used a new code for the computation and fitting of the time-lags spectra, KYNXILREV. The code is publicly avail-

able, and it can be used to fit time-lags in XSPEC. The main advantage over the previous code (KYNREFREV, presented in G18) is that we use the recent XILLVER-D tables (García & Kallman 2010; García et al. 2013, 2016), and that we can let the disc density as a free parameter in the fit.

We estimated the time-lags between the 0.3-1 and 1-4 keV bands, and we extracted the energy spectrum in the 3-10 keV band. The time-lags are sensitive to the variability of the X-ray reflection component at low energies (i.e. of the variable soft excess), without being affected by the presence of an additional, black-body-like component, and of the warm absorber, as long as these components do not vary on short time scales. On the other hand, the energy spectrum in the 3-10 keV band should be dominated by the main reflection feature in this band, i.e. the broad iron line. So, with our approach we can examine whether both the iron line and the soft-excess are consistent with the X-ray reverberation hypothesis, and constrain better the disc/corona properties.

Moreover, we estimated and fitted (simultaneously) the time-lags and energy spectrum in three separate flux periods (low, medium and high-flux). To the best of our knowledge, this is the first time, for an AGN, that both the energy and the time-lags spectra are fitted in different flux periods. Our results are in agreement with the results of Jiang et al. (2018) and Alston et al. (2020). We find a positive correlation between the corona height and the continuum flux, like Alston et al. (2020), and we show that the energy spectra in the three different flux states are fully consistent with the variation of the corona height with source flux. We find an electron disc density of  $n_e \sim 2.5 \times 10^{18} \text{ cm}^{-3}$  and an iron abundance of  $\sim 5 Z_\odot$ , like Jiang et al. (2018), and we show that the time-lags are fully consistent with these disc properties. We find a best fit inclination of  $\sim 45 - 50^\circ$ , which is smaller than what Jiang et al. (2018) found, and more consistent with what is usually assumed for Type 1 AGNs. Finally, our model fitting results strongly suggest that the BH spin is close to 1 in IRAS 13224-3809.

The simultaneous fit of the timing/spectral properties constitutes a complete approach, and provides a “unified” picture of the inner region in this AGN. Our work confirms that the results that have been reported from the study of either the energy or of the time-lags spectrum are indeed valid for both of them. Furthermore, by fitting simultaneously timing and spectral products, we can determine the disc/corona parameters more accurately. We believe that our results, together with the results from previous works (i.e. Chainakun et al. 2016 and Chainakun & Young (2017)), reinforce the belief of the community that a combined timing/spectral fit can indeed provide a complete description of the processes, properties and the inner geometry of AGN. As new models and codes become publicly available, this possibility should start to be the common in the future.

We discuss below some implications of the results we obtained from our analysis.

### 5.1 The BH spin

Following G18, we fitted the data by assuming either a rapidly spinning ( $a = 0.99$ ) or a non-rotating BH ( $a = 0$ ). The idea is to investigate whether the existing data can indicate that one option is significantly better than the other. G18 found that, by modelling the time-lags only of three AGN (excluding IRAS 13224-3809), it is not possible to discern between these two cases. A major result of our current study is that a (rapidly) spinning BH gives a significantly better fit to the time-lags and energy spectra. This is probably

due to the fact that IRAS 13224-3809 has the best observations so far for this kind of X-ray reverberation studies.

Although the model in the  $a = 0$  case can fit the energy spectra as well as the  $a = 0.99$  case (see the right panels in Fig. 4), it systematically underestimates the (negative) time-lags at frequencies above  $\sim 3 \times 10^{-4} \text{ Hz}$  (see the upper left panel in the same figure). In fact the  $a = 0$  model cannot adjust freely the disc density and the corona height to fit the time-lags equally well as the  $a = 0.99$  solution, mainly due to the time-lag spectral feature. The energy spectra, even though featureless, allowed us to find the values of the photon index and the observed luminosity for each flux period that helped us to well-constrain the final solution of the fitting process. These results show the strength of the combined spectral/timing model fitting. The constraints of the model are very restrictive in our work, as we fit time-lags and energy spectra, simultaneously in three flux periods. Although we cannot estimate the BH spin with any accuracy, our results strongly indicate that the BH in IRAS 13224-3809 is rotating.

### 5.2 The height of the X-ray source

We find the corona height to increase with increasing X-ray luminosity. Our best fit results suggest an X-ray height of  $\sim 3.5$  and  $\sim 5.5 r_g$ , when the observed 2-10 keV X-ray luminosity is of  $\sim 1.4$  and  $\sim 2.7$  percent of the  $L_{\text{Edd}}$  (i.e. during the LF and MF periods, respectively). The height of the source increases to almost  $\sim 10 r_g$  in the HF period, when the X-ray luminosity is  $\sim 5.5$  percent of the Eddington limit. In fact, this change in the height of the source, if real, can explain (in part) the extreme observed X-ray variability amplitude of the source. We estimate the *intrinsic* X-ray luminosity to vary from  $\sim 7$  to  $\sim 9$  percent of the  $L_{\text{Edd}}$  (in the LF and HF period, respectively), which is rather small compared to the observed light curve amplitude variation.

IRAS 13224-3809 is the first AGN where flux-related time-lags variations were detected (Kara et al. 2013). In this work we confirm the previous claim by Kara et al. (2013) that the X-ray source may be located closer to the accretion disc in the lower-flux than during the high flux periods. Our best model-fits suggest that flux related height variations can explain the time-lags in various flux periods, similar to what Kara et al. (2013) proposed for the time-lags variations during flaring and quiescent periods. Our results are fully consistent with Alston et al. (2020), who studied the same source, using (almost) the same observations. These authors studied the time-lags only, using a previous version of the X-ray reverberation code that the one we use in this work. They estimated the time-lags using the data from single *XMM-Newton* orbits, and they found that the time-lags are best fitted when the height of the X-ray corona increases with increasing X-ray flux. We studied the time-lags simultaneously with the energy spectra, in three broader flux periods. The loss in time “resolution” of the time-lags evolution in our study is somehow counter-balanced by the use of the energy spectra. In both studies the results are the same: assuming the lamp-post hypothesis, the height of the X-ray source increases by a factor of  $\sim 3$  when the observed X-ray luminosity appears to increase by factor of  $\sim 4$ .

The height of the X-ray corona appears to be  $\sim 3 - 5 r_g$  when the source is in the LF and MF period, but then it increases by a factor of two (at least) when the source is in the HF period. Fig. 1 shows that the source spends less time in the HF period, which is characterized by very fast, “spiky”, flare-like events. These are similar to the “spiky” flares in the simulations of Ghisellini et al. (2004), in the case of the “aborted jet” scenario for the X-ray emis-



sion in radio-quiet AGN (see for example the figures 4 and 7 in their paper). According to these authors the X-ray emission is due to “blobs” of material, which can reach a maximum radial distance and then fall back, colliding with the blobs produced later and still moving outwards. Possibly the large source height during the HF periods may be due to collisions that happened at higher heights either because the blobs have a larger initial velocity or they are launched at larger distances from the BH (both assumptions result in the same effect, see §5.2 in Ghisellini et al. 2004). At the same time, if the width of these blobs increases as they move (due to expansion) their dissipation time scale will also increase (eq. 23 in Ghisellini et al. 2004), which could also explain the decrease on the characteristic break frequency in the PSD of the source with increasing source flux (Alston et al. 2019).

We furthermore note that the best-fit residuals of the HF time-lags have a wavy-like appearance. The wavy-residuals are not significant (the best-fit  $\chi^2$  to the time-lags of the spectrum in the HF period is statistically acceptable), but we find their presence intriguing. G18 had also observed wavy-residuals in the time-lags spectra of the three AGN they had studied, as well as Chainakun & Young (2017) in the case of PG 1244+026. These residuals cannot be explained in the case of the simple lamp-post geometry, but as Chainakun & Young (2017) suggested, they might be indicative of the presence of two, co-axial point sources. This is an interesting possibility, which could suggest that, when in the HF state, both a large and lower height sources may co-exist in IRAS 13224-3809, with the lower height source being fainter. An alternative explanation for these wavy residuals was recently proposed by Chainakun et al. (2019). These authors considered that the time-lags would be produced in the case of a spherical corona, and they showed that the bumps and wiggles in the time-lags should be present in this case. They also found stronger wiggles when the corona is optically thicker, or when it becomes larger. It might be that the corona expands in IRAS 13224-3809 as its height increases, producing this wavy pattern in the observed time-lags spectra.

## ACKNOWLEDGMENTS

MCG, MD and VK acknowledge the support by the project RVO:67985815 and GACR project 18-00533S. MCG acknowledges funding from ESA through a partnership with IAA-CSIC (Spain).

## DATA AVAILABILITY

The KYNXILREV and KYNXILLVER codes used to fit the data are publicly available at:

<https://projects.asu.cas.cz/stronggravity/kynreverb/>

and

<https://projects.asu.cas.cz/stronggravity/kyn/>

All the data presented in this paper are available upon (reasonable) request.

## REFERENCES

Akaike, H., 1973, in Petrov B. N., Csaki F., eds, Second International Symposium on Information Theory. Akadémiai Kiado, Budapest, p. 267  
Alston, W. N., Fabian, A. C., Buisson, D. J. K. et al., 2019, MNRAS, 482, 2088

Alston, W. N., Fabian, A. C., Kara, E., et al., 2020, *astro-ph/2001.06454*  
Arnaud, K. A. (1996), *Astronomical Society of the Pacific Conference Series*, 101, 17  
Boller, Th., Brandt, W. N., Fabian, A. C. et al., 1997, MNRAS, 289, 393  
Boller, Th., Tanaka, Y., Fabian, A., et al., 2003, MNRAS, 343, 89  
Caballero-García, M. D., Papadakis, I. E., Dovčiak, M. et al., 2018, MNRAS, 480, 2650 (G18)  
Cackett, E. M., Zoghbi, A., Reynolds, C. et al., 2014, MNRAS, 438, 2980  
Chainakun, P. & Young, A. J., 2015, MNRAS, 452, 333  
Chainakun, P., Young, A. J. & Kara, E., 2016, MNRAS, 460, 3076  
Chainakun, P. & Young, A. J., 2017, MNRAS, 465, 3965  
Chainakun, P., Watcharangkool, A., Young, A. J. & Hancock, S., MNRAS, 487, 667  
Chartas, G., Rhea, C., Kochanek, C. et al., 2016, AN, 337, 356  
Chartas, G. & Canas, M. H., 2018, ApJ, 867, 103  
Chiang, Chia-Ying, Walton, D. J., Fabian, A. C., 2015, MNRAS, 446, 759  
Dauser, T., Garcia, J., Parker, M. L., et al., 2014, MNRAS, 444L, 100  
De Marco, B., Ponti, G., Cappi, M. et al. (2013), MNRAS, 431, 2441  
Dewangan, G. C., Boller, Th., Singh, K. P. et al., 2002, A&A, 390, 65  
Dovčiak, M., Karas, V. & Yaqoob, T., 2004, ApJS, 153, 205  
Dovčiak, M., Svoboda, J., Goosmann, R. W. et al., *Proceedings of RAGtime 14-16*, 2014, 51  
Emmanoulopoulos, D., McHardy, I. M., Papadakis, I. E. (2011) MNRAS, 416, 94  
Emmanoulopoulos, D., Papadakis, I. E., Dovčiak, M. & McHardy, I. M., 2014, MNRAS, 439, 3931  
Emmanoulopoulos, D., Papadakis, I. E., Epitropakis, A., Pecháček, T., Dovčiak, M. et al., 2016, MNRAS, 461, 1642  
Epitropakis, A., Papadakis, I. E., Dovčiak, M. et al., 2016, A&A, 594, 71  
Epitropakis, A. & Papadakis, I. E. (2016) A&A, 591, 113  
Epitropakis, A. & Papadakis, I. E., 2017, MNRAS, 468, 3568  
Fabian, A. C., Zoghbi, A., Ross, R. R. et al. (2009), Nature, 459, 540  
Fabian, A. C., Kara, E., Walton, D. J. et al., 2013, MNRAS, 429, 2917  
Gabriel C., et al., 2004, in Ochsenbein F., Allen M. G., Egret D., eds., *Astronomical Society of the Pacific Conference Series Vol. 314, Astronomical Data Analysis Software and Systems (ADASS) XIII*. p. 759  
Gallo, L. C., Boller, Th., Tanaka, Y. et al., 2004, MNRAS, 347, 269  
García & Kallman (2010), ApJ, 718, 695  
García, J., Dauser, T., Reynolds, C. S. et al., 2013, ApJ, 768, 146  
García, Javier A., Fabian, Andrew C., Kallman, et al., 2016, MNRAS, 462, 751  
Ghisellini, G., Haardt, F. & Matt, G., 2004, A&A, 413, 535  
Jiang, J., Parker, M. L., Fabian, A. C., 2018, MNRAS, 477, 3711  
Kara, E., Fabian, A. C., Cackett, E. M. et al., 2013, MNRAS, 430, 1408  
Kara, E., Alston, W. N., Fabian, A. C. et al. (2016), MNRAS, 462, 511  
Lumb, D., Warwick, R. S., Page, M., & de Luca, A. 2002, A&A, 389, 93  
McHardy, I. M., Koerding, E., Knigge, C., 2006, Natur, 444, 730

- McHardy, I. M., Arévalo, P., Uttley, P., et al.(2007), MNRAS, 382, 985
- Mushotzky, R. F., 1982, ApJ, 256, 92
- Parker, M. L., Alston, W. N., Buisson, D. J. K. et al., 2017, MNRAS, 469, 1553
- Parker, M. L., Matzeu, G. A., Guainazzi, M. et al., 2018, MNRAS, 480, 2365
- Pinto, C., Alston, W., Parker, M. L. et al., 2018, MNRAS, 476, 1021
- Ponti, G., Gallo, L. C., Fabian, A. C. et al., 2010, MNRAS, 406, 2591
- Strüder, L., Briel, U., Dennerl, K. et al., 2001, A&A, 365L, 18
- Turner, M. J. L., Abbey, A., Arnaud, M. et al., 2001, A&A, 365, 27

This paper has been typeset from a  $\text{\TeX}$ / $\text{\LaTeX}$  file prepared by the author.